

# Oscillation threshold of a Raman clarinet with localized nonlinear losses at the open end

Nathan Szwarcberg,<sup>1,2, a</sup> Tom Colinot,<sup>1</sup> Christophe Vergez,<sup>2</sup> and Michaël Jousserand<sup>1</sup>

<sup>1</sup>*Buffet Crampon, 5 Rue Maurice Berteaux, 78711 Mantes-la-Ville, France*

<sup>2</sup>*Aix Marseille Univ, CNRS, Centrale Med, LMA, Marseille, France*

Localized nonlinear losses are taken into account in a simple Raman clarinet model. The complete system is expressed as an iterated map, enabling to study the stability of the different playing regimes. A parametric study is carried out with respect to three major parameters: blowing pressure, embouchure and nonlinear losses coefficient. The model exhibits the well-known effect of reducing the maximum blowing pressure until the oscillations stop (extinction threshold) when nonlinear losses increase. Furthermore, the stability analysis also shows that increasing nonlinear losses increases the minimal blowing pressure for which the oscillations start (oscillation threshold).

[<https://doi.org/DOI number>]

[XYZ]

Pages: 1–11

## I. INTRODUCTION

The Raman model can be considered as one of the simplest physical models of clarinet<sup>1</sup>. It is composed of a reed which behaves as an idealized spring with no other dynamics, and of a passive resonator characterized by its reflection function. Viscothermal losses are neglected or reduced to a constant coefficient<sup>2</sup> independent from the frequency. The motion of the reed is coupled to the response of the resonator through the nonlinear characteristic of the flow crossing the reed channel<sup>3</sup>, enabling the system to produce self-sustained oscillations.

In spite of its simplicity, the Raman clarinet model is useful in that it can provide valuable insights on the behavior of a real instrument. The model predicts experimental results on the position and nature of the oscillation and extinction thresholds<sup>4–6</sup>, which are the minimal and maximal blowing pressures enabling self-sustained oscillations. Moreover, when the blowing pressure is increased linearly in time, experimental and numerical results both highlight a delay in the onset of the oscillation threshold<sup>7</sup>. This delay indicates a sensitivity of the system to dynamic bifurcations<sup>8</sup>. Finally, the influence of localized nonlinear losses at the end of the resonator on the extinction threshold has been demonstrated by a comparison between experiments and simulations with a modified Raman model<sup>4,6</sup>.

Although the influence of localized nonlinear losses on the dynamic behavior of the clarinet is documented for very high blowing pressure<sup>4,6,9</sup>, their influence over the global range of control parameters is less well known. Keefe (1983)<sup>10</sup> points out that it is more difficult for a clarinetist to maintain a stable oscillating regime when the contribution of localized nonlinear losses in a tone hole is higher. This observation invites us to study the

stability of a simple modified Raman model made of a cylindrical tube with localized nonlinear losses at the open end.

The complete model accounting for nonlinear losses located at the open end of the tube is defined in section II. The system is studied as an iterated map<sup>2,11</sup>. Thus, the stability of the different regimes can be easily computed with respect to the blowing pressure, the embouchure parameter and the nonlinear losses coefficient. The method to study the stability of the different regimes is recalled in section III. The influence of localized nonlinear losses on the stability of the equilibrium and on the two-state regime is studied in section IV. Other long-period regimes are also investigated. Finally, in section V, the influence of localized nonlinear losses on the dynamics of the clarinet is compared with that of linear losses. Possible implications for the musician are discussed.

## II. MODEL

A cylindrical tube is considered of length  $L$ , radius  $a$  and cross-section  $S$ . The characteristic impedance of plane waves in the tube is  $Z_c = \rho_0 c_0 / S$ , where  $\rho_0 = 1.23 \text{ kg}\cdot\text{m}^{-3}$  is the density of air, and  $c_0 = 343 \text{ m}\cdot\text{s}^{-1}$  is the speed of sound in the air. The position along the main axis of the tube is indicated by  $x \in [0, L]$ .

### A. Resonator

The acoustic pressure  $p(x, t)$  is defined as the sum of a traveling wave  $p^+(x, t)$  and a regressive wave  $p^-(x, t)$ :

$$p(x, t) = p^+(x, t) + p^-(x, t). \quad (1)$$

The acoustic velocity  $v(x, t)$  is defined from  $p^+$  and  $p^-$  as

$$\rho_0 c_0 v(x, t) = p^+(x, t) - p^-(x, t). \quad (2)$$

The acoustic flow  $u$  is also defined so that  $u = Sv$ .

<sup>a</sup>[nathan.szwarcberg@buffetcrampon.com](mailto:nathan.szwarcberg@buffetcrampon.com)

In the Raman model, viscothermal losses do not depend on the frequency<sup>2</sup>. Thus in the time domain, the transmission line along the tube is given by

$$\begin{cases} p^+(L, t) = \lambda p^+(0, t - L/c_0) \\ \lambda p^-(L, t - L/c_0) = p^-(0, t), \end{cases} \quad (3)$$

where  $\lambda \in [0, 1]$ . It can be shown that in the Raman model, increasing the dissipation due to radiation at the open end of the tube is equivalent to reducing  $\lambda$ : losses due to propagation and localized linear losses due to radiation are indistinguishable.

## B. Boundary condition for the localized nonlinear losses

In this section, for reading comfort,  $p^+(L, t)$  and  $p^-(L, t)$  are written as  $p^+$  and  $p^-$ . The same applies for  $p$  and  $v$ .

Localized nonlinear losses are related to the dissipation of the turbulent flow at the exit of the tube, which can take the form of vortices for high acoustic velocities<sup>12</sup>. They are accounted for through the following relationship at  $x = L$ , assuming a quasi-stationary flow<sup>6,13,14</sup>:

$$p = \rho_0 C_{\text{nl}} v |v|, \quad (4)$$

where  $C_{\text{nl}} \geq 0$  is a dimensionless constant which characterizes the vena-contracta of the jet. Its value increases when the sharpness of the edges at the open end of the tube increases. Moreover, it does not depend on the diameter of the tube<sup>15</sup>. Theoretically, the maximum value of the nonlinear losses coefficient is  $C_{\text{nl}} = 0.5$  (often written  $c_d = 4 \cdot C_{\text{nl}} = 2$ ) for a monochromatic wave. This theoretical boundary applies to an unflanged tube with thin walls and sharp edges<sup>16</sup>. However, Atig *et al.* (2004)<sup>6</sup> and Dalmont and Frappé (2007)<sup>4</sup> find a best fit on experimental results for  $C_{\text{nl}} = 0.7$  ( $c_d = 2.8$ ), for a clarinet with an unflanged termination with sharp edges. As explained by Dalmont and Frappé (2007)<sup>4</sup>, this overestimation can first be due to the nature of the acoustic field in the clarinet which is significantly different from a sine wave, and also to the fact that in the Raman model, linear losses are underestimated for higher frequencies.

To suit the reflection function formalism, the boundary condition (4) has to be rewritten by an explicit relationship between  $p^-$  and  $p^+$ . An elegant method to solve this problem is proposed by Monteghetti (2018, Chap. 2.4.2)<sup>17</sup>. In the present article, another and more straightforward method is employed by substituting directly  $p^+$  and  $p^-$  in Eq. (4) through Eqs. (1) and (2). Two quadratic polynomials in  $p^-$  are obtained after this substitution:

$$\begin{aligned} (p^-)^2 - (2p^+ + K^{-1})p^- + (p^+ - K^{-1})p^+ &= 0 \text{ if } p^+ \geq p^-, \\ (p^-)^2 - (2p^+ - K^{-1})p^- + (p^+ + K^{-1})p^+ &= 0 \text{ if } p^+ \leq p^-, \end{aligned}$$

where  $K = C_{\text{nl}}/(\rho_0 c_0^2)$ . The solution of each of these two equations in  $p^-$  is:

$$\begin{aligned} p^- &= p^+ + \frac{1}{2K} \left( 1 - \sqrt{1 + 8Kp^+} \right) \quad \text{if } p^+ \geq 0, \\ p^- &= p^+ + \frac{1}{2K} \left( -1 + \sqrt{1 - 8Kp^+} \right) \quad \text{if } p^+ \leq 0. \end{aligned}$$

By combining the two conditions on  $p^+$ , the following expression is obtained for the reflection at the open end:

$$p^- = p^+ + \frac{1}{2K} \frac{p^+}{|p^+|} \left( 1 - \sqrt{1 + 8K|p^+|} \right).$$

After a bit of algebra, the following expression is finally obtained:

$$p^- = p^+ \left( 1 - \frac{4}{1 + \sqrt{1 + K_L|p^+|}} \right), \quad (5)$$

with  $K_L = 8C_{\text{nl}}/(\rho_0 c_0^2)$ . The reflection function at  $x = 0$  is deduced by substitution of Eq. (3) in Eq. (5):

$$p^-(0, t) = r_{\text{nl}}[p^+(0, t - \tau)], \quad \text{where} \quad (6)$$

$$r_{\text{nl}}(\xi) = \lambda^2 \xi \cdot \left( 1 - \frac{4}{1 + \sqrt{1 + K_0|\xi|}} \right), \quad (7)$$

with  $K_0 = \lambda K_L$  and  $\tau = 2L/c_0$ . It can be checked that the reflection function is passive, i.e for all  $t > 0$  and  $\xi \in \mathbb{R}$ :

$$\int_{-\infty}^t |[r_{\text{nl}}(\xi)](t)|^2 dt \leq \int_{-\infty}^t |\xi(t)|^2 dt.$$

The reflection function (under its dimensionless form) is represented on Figure 1 for different values of  $K_0 \in [0, \infty]$ . Increasing nonlinear losses results in a continuous transformation from the boundary condition of an open tube (in blue) to that of a closed tube (in red). This transformation is symmetrical with respect to the point (0, 0).

Note that the computation of the reflection function leads to a different result from Eq. (22) of Atig *et al.* (2004)<sup>6</sup>. It can be checked that the expression from Atig *et al.* (2004)<sup>6</sup> is derived from Eq. (5) by expanding  $p^+$  to the first order around zero.

## C. Nonlinear characteristic and complete model

The flow entering the bore through the reed channel is given by the well-known nonlinear characteristic<sup>11</sup>:

$$\hat{u}(t) = \zeta [\hat{p}(t) - \gamma + 1]^+ \text{sgn}[\gamma - \hat{p}(t)] \sqrt{|\gamma - \hat{p}(t)|}, \quad (8)$$

where  $[\xi]^+ = \xi \cdot \text{Heaviside}(\xi)$ ,  $\gamma > 0$  is the dimensionless blowing pressure, and  $\zeta \in [0, 1]$ <sup>11</sup> is the embouchure parameter. The dimensionless input pressure and flow are noted  $\hat{p}(t) = p(0, t)/P_M$  and  $\hat{u}(t) = u(0, t)Z_c/P_M$ , where  $P_M \in [4, 8.5]$  kPa<sup>4,6</sup> is the minimal reed closing pressure.

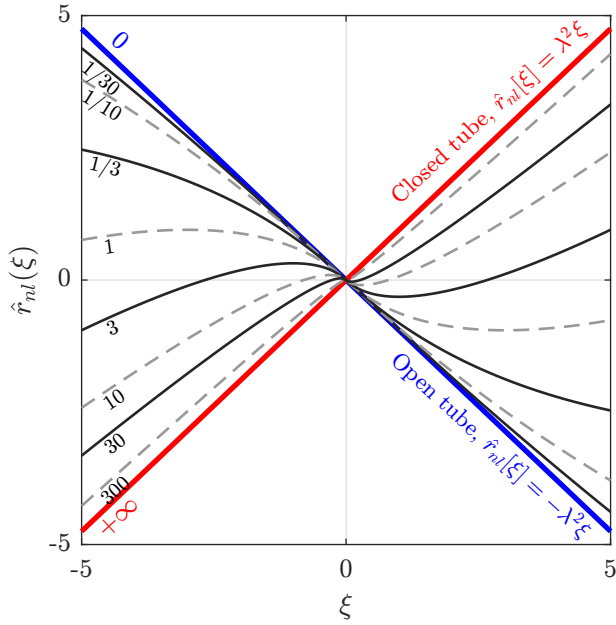


FIG. 1. Evolution of the shape of  $\hat{r}_{nl}$  when increasing  $\hat{K}_0$  (values are displayed on the figure), with  $\lambda = \sqrt{0.95}$ .

The expression of the nonlinear characteristic (8) as an explicit relationship between  $p^+$  and  $p^-$  can be found in Taillard *et al.* (2010, Appendix A)<sup>11</sup> by setting:

$$\begin{aligned} X &= \gamma - \hat{p} = \gamma - \hat{p}^+ - \hat{p}^- \\ Y &= \hat{u} + X = \gamma - 2\hat{p}^-. \end{aligned}$$

The nonlinear characteristic can be written as follows:

$$\begin{aligned} Y &= X & \text{if } X > 1; \\ Y &= X + \zeta(1 - X)\sqrt{X} & \text{if } 0 < X < 1; \\ Y &= X - \zeta(1 - X)\sqrt{-X} & \text{if } X < 0. \end{aligned}$$

The inverse function  $X(Y) = Y^{-1}(X)$  is determined by the same authors. From the definition of  $X$ , one can write:

$$\hat{p}^+(t) = \gamma - X(Y) - \hat{p}^-(t).$$

By substitution of  $r_{nl}$  [Eq. (7)] in  $\hat{p}^-(t)$ , the complete system is summarized in the following expression:

$$\hat{p}^+(t) = f(\hat{p}^+(t - \tau)), \quad \text{where} \quad (9)$$

$$f(\xi) = \gamma - X(\gamma - 2\hat{r}_{nl}(\xi)) - \hat{r}_{nl}(\xi) \quad \text{and} \quad (10)$$

$$\hat{r}_{nl}(\xi) = \lambda^2 \xi \cdot \left( 1 - \frac{4}{1 + \sqrt{1 + \hat{K}_0 |\xi|}} \right), \quad (11)$$

with  $\hat{K}_0 = P_M K_0$ . These formulas could be used in a delay-line formalism similar to Guillemain and Terroir (2006)<sup>18</sup>. In the following, Eq. (9) is written as an iterated function:  $\hat{p}_{n+1}^+ = f(\hat{p}_n^+)$ , with a time increment of

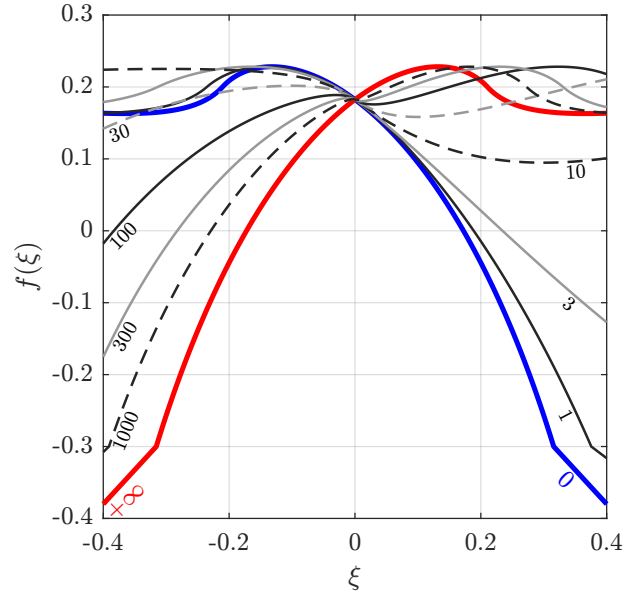


FIG. 2. Evolution of  $f$  when increasing  $\hat{K}_0$  (values are displayed on the figure), with  $\lambda = \sqrt{0.95}$ ,  $\gamma = 0.4$  and  $\zeta = 0.5$ .

$\tau$ . In the following, for conciseness,  $\hat{p}_n^+$  is denoted as  $x_n$  so that  $f(x_n) = x_{n+1}$ .

The iterated function is represented on Figure 2, for  $\lambda = \sqrt{0.95}$ ,  $\gamma = 0.4$ ,  $\zeta = 0.5$  and increasing values of  $\hat{K}_0$  from the open tube ( $\hat{K}_0 = 0$ ) to the closed tube ( $\hat{K}_0 \rightarrow +\infty$ ) boundary conditions. All curves cross the point  $(0, f(0))$  since  $\hat{r}_{nl}(0) = 0$ . Moreover, the curves for  $\hat{K}_0 = 0$  and  $\hat{K}_0 = +\infty$  are symmetrical with respect to the axis  $\xi = 0$ , since  $\hat{r}_{nl}(\xi)$  for  $\hat{K}_0 = 0$  is equal to  $\hat{r}_{nl}(-\xi)$  for  $\hat{K}_0 = +\infty$ .

According to the experimental results from Atig *et al.* (2004)<sup>6</sup> and Dalmont and Frappé (2007)<sup>4</sup>, the maximum value of the localized nonlinear losses coefficient would be  $\hat{K}_0 = 0.325$ , for  $C_{nl} = 0.7$ ,  $P_M = 8.5$  kPa and  $\lambda = \sqrt{0.95}$ . The motivation to study values of  $\hat{K}_0$  that are far higher than observed experimental results is in line with the very simple formalism of the iterated functions, which calls for an exhaustive study of the space of the control parameters. Furthermore, exploring the behavior of the clarinet for very high values of  $\hat{K}_0$  is meaningful when nonlinear losses are localized in the side holes of a woodwind. As stated in Chapter 8.4.5.2 of Chaigne and Kergomard (2016)<sup>1</sup>: “if the, even real, impedance of a side hole, increases notably, it may eventually act as a closed end for the hole!”

### III. METHODS

The properties of the iterated function are thoroughly described by Taillard *et al.* (2010)<sup>11</sup>. A few notions are recalled here to study the stability of the different regimes.

Function  $f$  is an iterated function, meaning that

$$x_{n+k} = \underbrace{(f \circ f \circ \dots \circ f)}_{k \in \mathbb{N}^*}(x_n) = f^{(k)}(x_n).$$

For a given set of control parameters  $(\gamma, \zeta, \hat{K}_0, \lambda)$ , a fixed point  $x^*$  of  $f$  is considered, so that

$$f(x^*) = x^*.$$

From the practical point of view,  $f$  is sampled over a vector  $\mathbf{x}$  with  $N_x$  values  $x_i$  linearly spaced within the range  $x_i \in [-\gamma - 0.1, \gamma + 0.1]$  (the boundaries are chosen empirically to ensure that all fixed points are found for all values of the control parameters considered). The fixed point  $x^*$  is computed by linear interpolation of the zero-crossing of  $f(\mathbf{x}) - \mathbf{x}$ . The choice of linear interpolation is preferred since the iterates  $f^{(k)}$  have many discontinuities on their derivatives. The fixed point is stable if

$$|f'(x^*)| < 1,$$

where  $f' = \partial_x f$ . Furthermore, if  $x_k^*$  is a fixed point of  $f^{(k)}$ , then it is also a fixed point for every iterate  $f^{(nk)}$  with  $n \in \mathbb{N}^*$ . If  $x_k^*$  is stable (resp. unstable) for the iterate  $f^{(k)}$ , then it is also stable (resp. unstable) for every higher iterates  $f^{(nk)}$ . In this study, the stability of the following regimes is considered.

1. The equilibrium (non-oscillating state, denoted  $R_1$ ) associated to a fixed point  $x_1^*$  of  $f$ , which is stable if  $x_1^*$  is stable with respect to  $f$ .
2. The two-state (or quarter-wavelength) regime, denoted  $R_2$ , which is stable if two fixed points  $x_2^*$  of  $f^{(2)}$  that are different from  $x_1^*$  are stable with respect to  $f^{(2)}$ . An example is shown on the first row of Suppl. Fig. 1.
3. The long-period regime ( $R_n$ ), which is stable if  $n$  fixed points  $x_n^*$  of  $f^{(n)}$  are stable with respect to  $f^{(n)}$  and are different from the fixed points of  $f^{(k)}$ , where  $k$  are divisors of  $n$ . In this article, only the regimes  $R_3, R_4, R_6$  and  $R_8$  are studied. Examples of three-state and four-state regimes are provided on the second and third row of Suppl. Fig. 1.

To compute the stability of the different regimes of interest, the control parameters space  $(\gamma, \zeta, \hat{K}_0, \lambda)$  is meshed on a regular grid. The ranges of the parameters and their associated step sizes are given in Table I. For the simulations leading to the results presented in sections IV and VA 2, the linear losses parameter is fixed at  $\lambda = \sqrt{0.95}$  to reduce the problem to three dimensions and simplify the representation of the results. The value of  $\lambda$  is chosen to be consistent with Taillard *et al.* (2010)<sup>11</sup>. For a detailed study about the sensitivity of the Raman model to  $\lambda$ , see Taillard and Kergomard (2015)<sup>19</sup> and section VA 1.

For every set of control parameters, the fixed points of  $f, f^{(2)}$  and  $f^{(n)}$  are computed. The stability of the corresponding regimes is then determined.

TABLE I. Ranges and step sizes of the control parameters used in the simulations.

Parameter	Min	Max	Step size
$\gamma$	0	5	$10^{-3}$
$\zeta$	0.01	0.99	$5 \cdot 10^{-3}$
$\lambda$	0.1	1	$5 \cdot 10^{-3}$
$\hat{K}_0$	0	100	$5 \cdot 10^{-2}$

## IV. RESULTS

### A. Oscillation threshold

The region in which the equilibrium  $R_1$  is stable is represented in the  $(\gamma, \zeta, \hat{K}_0)$  space on Figure 3. Different views and cross-sections are given in the Supplementary Figure 2. When  $\hat{K}_0 = 0$ , the well-known oscillation threshold curve is recognized in the  $(\gamma, \zeta)$  hyperplane<sup>4,20</sup>. The threshold  $\gamma_{\text{osc} \searrow}$  at which the oscillations start when decreasing the blowing pressure from a reed blocked against the mouthpiece (sometimes named ‘‘inverse threshold’’<sup>4</sup>) is also visible at  $\gamma = 1$ . When  $\hat{K}_0$  increases, the oscillation threshold (noted  $\gamma_{\text{osc} \nearrow}$ ) shifts to higher values of  $\gamma$  while the inverse threshold stays at  $\gamma = 1$ . The three cuts represented by dashed lines show that for  $\hat{K}_0 = \{1, 5, 10\}$ , the average oscillation threshold (computed for  $\zeta > 0.2$ ) is respectively at  $\gamma \approx \{0.40, 0.60, 0.73\}$ . When  $\hat{K}_0 > 34$ , the region of stability of  $R_1$  begins to extend also along the  $\zeta$  dimension. Finally, when  $\hat{K}_0 \rightarrow +\infty$ , the equilibrium is stable everywhere in the  $(\gamma, \zeta)$  space for  $\gamma < 1$ .

### B. Extinction threshold and stability of the two-state regime above $\gamma = 1$

The stability region of the two-state regime  $R_2$  is represented on Figure 4, in the  $(\gamma, \zeta)$  plane, for  $0 \leq \hat{K}_0 \leq 2$ . This Figure is also represented in terms of measurable variables (blowing pressure, height of the reed at rest) in Suppl. Fig. 3. Above  $\gamma = 1$ , nonlinear losses greatly reduce the stability of  $R_2$ , especially for high values of  $\zeta$ . This effect is known and has been proven by numerical and experimental comparisons<sup>4,6</sup>. When  $\hat{K}_0 \rightarrow \infty$ ,  $R_2$  is unstable everywhere in the  $(\gamma, \zeta)$  space.

Furthermore, the effect of localized nonlinear losses on the extinction threshold is much more important than their effect on the oscillation threshold. For  $\hat{K}_0 = \{0, 0.325\}$  the oscillation threshold for  $\zeta = 0.3$  is located respectively at  $\gamma_{\text{osc} \nearrow} = \{0.378, 0.393\}$ , amounting to an increase of 4.0 %. In comparison, the value of the extinction threshold of  $R_2$  decreases by 40 % for the same set of control parameters. The effect of nonlinear losses is then ten times more important on the extinction threshold than on the oscillation threshold. This scale discrepancy can explain why the influence of localized nonlinear losses located at the open end of a tube is not mentioned in pre-

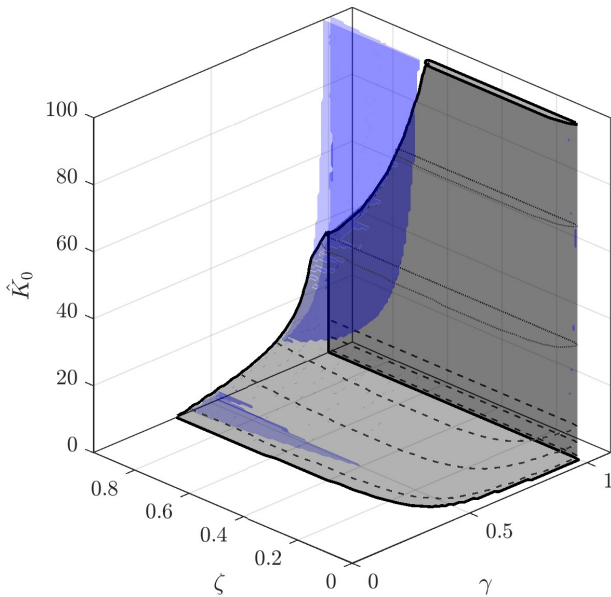


FIG. 3. Limit of stability of  $R_1$  (in black) and  $R_n$  ( $n > 2$ , in blue) in the  $(\gamma, \zeta, \hat{K}_0)$  space, for  $\lambda = \sqrt{0.95}$ . The non-oscillating state is stable outside the volume delimited by the black surface, and unstable inside. The three dashed-line curves are horizontal cuts at  $\hat{K}_0 = \{1, 5, 10\}$ . The two dotted-line curves are horizontal cuts at  $\hat{K}_0 = \{35, 70\}$ . The long-period regimes are unstable outside the volume delimited by the blue surface. Other views and cross-sections are shown in the Supplementary Figure 2.

vious studies<sup>4,9,21–23</sup>. In addition, in these studies, the difference in the onset of the oscillations might be masked by the bifurcation delay induced by the time-variation of  $\gamma$ <sup>7,8</sup>.

Finally, the presence of a small region around  $\gamma \approx 0.5$  where the two-state regime is unstable can be noted. As shown on the right panel of Figure 4, when  $\hat{K}_0$  increases from 0 to 2, the area where  $R_2$  is unstable shrinks towards high values of  $\zeta$ . For  $\hat{K}_0 = 0$ , a chaotic behavior exists around  $\gamma \approx 0.45$  for high values of  $\zeta$ <sup>11</sup>. In the case of  $\hat{K}_0 = 2$ , stable four-state and eight-state regimes are found.

### C. Long-period regimes

Regimes that are stable in either  $R_3$ ,  $R_4$ ,  $R_6$  and  $R_8$  are indicated by the volumes delimited by the blue surfaces on Figure 3. When  $\hat{K}_0 = 0$ , stable long-period regimes exist around  $\gamma = 0.5$ , as also shown on Figure 4. They progressively disappear when  $\hat{K}_0$  increases slightly. This reduction may contribute to the fact that period-doubling regimes ( $R_4$ ) are seldom observed on the clarinet. Note, however, that for  $\zeta < 0.4$  (a typical value for the clarinet<sup>4</sup>) there are no existing long-period regimes for  $\hat{K}_0 = 0$  and  $\lambda = \sqrt{0.95}$ , as shown on the detailed view of Figure 4.

From  $\hat{K}_0 = 9$  and above, long-period regimes reappear for very high values of  $\zeta$ , in a thin band of  $\gamma$  near the oscillation threshold. This band expands towards lower values of  $\zeta$  as  $\hat{K}_0$  increases. Above  $\hat{K}_0 = 34$ ,  $R_n$  becomes multistable with the equilibrium  $R_1$ : for a same set of control parameters,  $R_1$  and a long-period regime coexist and are both stable. Further computations show that above  $\hat{K}_0 = 100$ , this multistability zone expands towards lower values of  $\zeta$ , as the band of  $\gamma$  becomes narrower and closer to  $\gamma = 1$ . For example, at  $\hat{K}_0 = 500$ , for  $\gamma = 0.993$ , the equilibrium is the only existing regime  $\forall \zeta < 1$ . For  $\gamma = 0.994$ , a stable two-state regime emerges at  $\zeta = 0.12$ , and for  $\gamma = 0.995$ , a stable four-state regime appears at  $\zeta = 0.64$ . No stable oscillating regime is found for  $\hat{K}_0 \rightarrow \infty$  and  $\gamma < 1$ .

## V. DISCUSSION

### A. Comparison between linear and localized nonlinear losses

To better understand the influence of localized nonlinear losses on the dynamic behavior of a Raman clarinet, a parallel study between linear losses ( $\lambda$ ) and nonlinear losses ( $\hat{K}_0$ ) is carried out.

### 1. Linear losses

With regard to linear losses, an insightful result is presented in Figure 5 of Taillard and Kergomard (2015)<sup>19</sup>. This Figure describes the nature of the playing regimes and the type of the bifurcation at the onset of the oscillations, for an increasing blowing pressure ( $\gamma_{\text{osc}\nearrow}$ ) and a decreasing blowing pressure from  $\gamma > 1$  ( $\gamma_{\text{osc}\searrow}$ ). This description is made in the plane  $(\mu, \zeta)$ , where  $\mu = (1 - \lambda^2)/(1 + \lambda^2)$ .

The results from Taillard and Kergomard (2015)<sup>19</sup> are reproduced on Figure 5 with the method presented in Section III, for  $\hat{K}_0 = 0$  and the values of  $\gamma, \zeta, \lambda$  written in Table I. The different colors in the  $(\lambda, \zeta)$  plane describe the dynamic behavior of the clarinet (the x-axis is inverted). Four points A, B, C, D are added to Figure 5 to describe the different playing scenarios at  $\gamma_{\text{osc}\nearrow}$  and  $\gamma_{\text{osc}\searrow}$ . In the detail figures at the bottom right corner, the equilibrium  $R_1$  is represented in black/gray (resp. stable/unstable), and the two-state regime  $R_2$  is represented in red/light red (resp. stable/unstable).

In the white region in the bottom-right half of the plane, no sound can be played, for all values of  $\gamma$ . For low values of  $\lambda$  (points C and D), the green region points out that the bifurcation at  $\gamma_{\text{osc}\nearrow}$  is inverse: the musician can not shift continuously from silence to *pianissimo*, which can be considered as a drawback. Outside the green region, the bifurcation at  $\gamma_{\text{osc}\nearrow}$  is direct (i.e. this continuous shift is possible, as it can be seen for points A and B). The blue and red regions describe the type of the bifurcation at  $\gamma_{\text{osc}\searrow}$ . In the red region, the bifurcation is inverse (points A and C). In the blue region, it is direct (points B and D), which also means that no sound can be played for  $\gamma > 1$ . In the section 7.3 of Taillard and Kergomard (2015)<sup>19</sup>, the authors explain that a direct

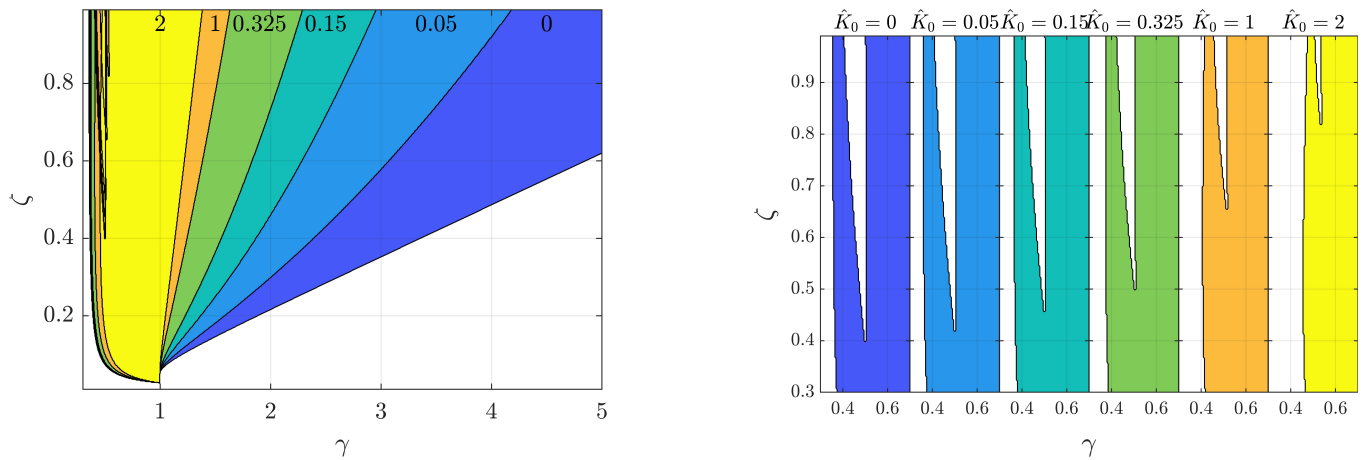


FIG. 4. Stability region of  $R_2$  in the  $(\gamma, \zeta)$  plane, for different values of  $\hat{K}_0 \in [0, 2]$  and  $\lambda = \sqrt{0.95}$ . The values of  $\hat{K}_0$  corresponding to the different colors are written on the figure. On the left panel, the color patches are superimposed in a fan shape from blue ( $\hat{K}_0 = 0$ ) to yellow ( $\hat{K}_0 = 2$ ). On the right panel, a detailed view is given on the region where  $R_2$  is unstable and  $R_n$  is stable.

bifurcation at  $\gamma_{\text{osc}\searrow}$  could be useful for the clarinetist since it “conducts to a clean *pianissimo*, with a sound richer in high harmonics” compared to the sound close to the threshold at  $\gamma_{\text{osc}\nearrow}$ . Finally, long-period regimes can be played in the yellow region, where  $\lambda$  is close to 1.

Figure 5 provides insights on the dynamic behavior of the clarinet, but lacks information regarding the playing range of the instrument with respect to the blowing pressure  $\gamma$ . For another viewpoint to compare linear losses and localized nonlinear losses, the playability of the instrument is represented in the  $(\lambda, \gamma)$  plane on Figure 6. For  $\lambda < 0.75$ , no long-period regimes (in yellow) can be played, as also shown on Figure 5. It can also be noticed that for  $\lambda \leq 0.6$ , sound can hardly be played for  $\gamma > 1$ . When  $\lambda \leq 0.39$ , Figure 5 shows that the bifurcation at  $\gamma_{\text{osc}\searrow}$  is direct for all  $\zeta$ : no sound can be played above  $\gamma = 1$ .

## 2. Localized nonlinear losses

The representation of Figures 5 and 6 is reproduced on Figures 7 and 8 for the nonlinear losses coefficient, with  $\lambda = \sqrt{0.95}$ . First and most importantly, it can be noticed on Figure 8 that for all  $\zeta \in [0, 0.99]$ , the oscillation threshold  $\gamma_{\text{osc}\nearrow}$  increases monotonically when  $\hat{K}_0$  increases. On the detailed view of Figure 8,  $\gamma_{\text{osc}\nearrow}$  increases from 0.36 to 0.41 when  $\hat{K}_0$  increases from 0 to 1. Moreover, Figure 7 shows that the equilibrium  $R_1$  becomes stable with at least one oscillating regime for high values of  $\zeta$  and  $\hat{K}_0 > 34$ , as illustrated on Figure 3.

Regarding the extinction threshold, Figure 8 highlights that nonlinear losses greatly decrease the value of the extinction threshold, for all  $\zeta \in [0, 0.99]$ . From  $\hat{K}_0 > 10$ , the extinction threshold is almost at  $\gamma = 1$ . Figure 7 also shows that the range where  $\gamma_{\text{osc}\searrow}$  is direct (i.e. the extinction threshold is located at  $\gamma = 1$ , repre-

sented in blue) increases linearly from  $\zeta \in [0.03, 0.05]$  for  $\hat{K}_0 = 0$  to  $\zeta \in [0.03, 0.13]$  for  $\hat{K}_0 = 100$ . Finally, regarding the long-period regimes, both Figure 7 and 8 show that stable long-period regimes exist for high values of  $\zeta$  and for all values of  $\hat{K}_0$ , except  $\hat{K}_0 \in [2, 8]$ .

The comparison between Figures 5 and 6 and Figures 7 and 8 highlights the following similarities and differences between linear and nonlinear losses. First, increasing linear losses and nonlinear losses both reduce the playing range of the clarinet by increasing the value of the oscillation threshold  $\gamma_{\text{osc}\nearrow}$  and reducing the value of the extinction threshold. Second, as the extinction threshold gets close to 1, the range in  $\zeta$  where the bifurcation at  $\gamma_{\text{osc}\searrow}$  is direct increases. Third, increasing linear and nonlinear losses both reduce the stability of the long-period regimes. For nonlinear losses, this observation is true for  $\hat{K}_0 < 8$ . Above this value, stable long-period regimes reappear. Finally, when linear losses are high ( $\lambda < 0.61$ ), the bifurcation at  $\gamma_{\text{osc}\nearrow}$  becomes inverse for all  $\zeta$ . This is not the case for nonlinear losses, where  $\gamma_{\text{osc}\nearrow}$  is always direct.

## B. Implications for the musician

Taillard and Kergomard (2015)<sup>19</sup> discuss that when linear losses increase, the reduction of the value of the extinction threshold could be useful for the musician to perform a “clean *pianissimo*”. Therefore, localized nonlinear losses might also be beneficial by enhancing this effect.

Increasing linear and nonlinear losses not only reduces the playing range of the clarinet, but also the amplitude of the acoustic pressure in the air column. This effect has already been studied experimentally<sup>4,6</sup> and numerically<sup>6,9,22</sup>. In comparison with linear losses, it is worth noting that localized nonlinear losses significantly

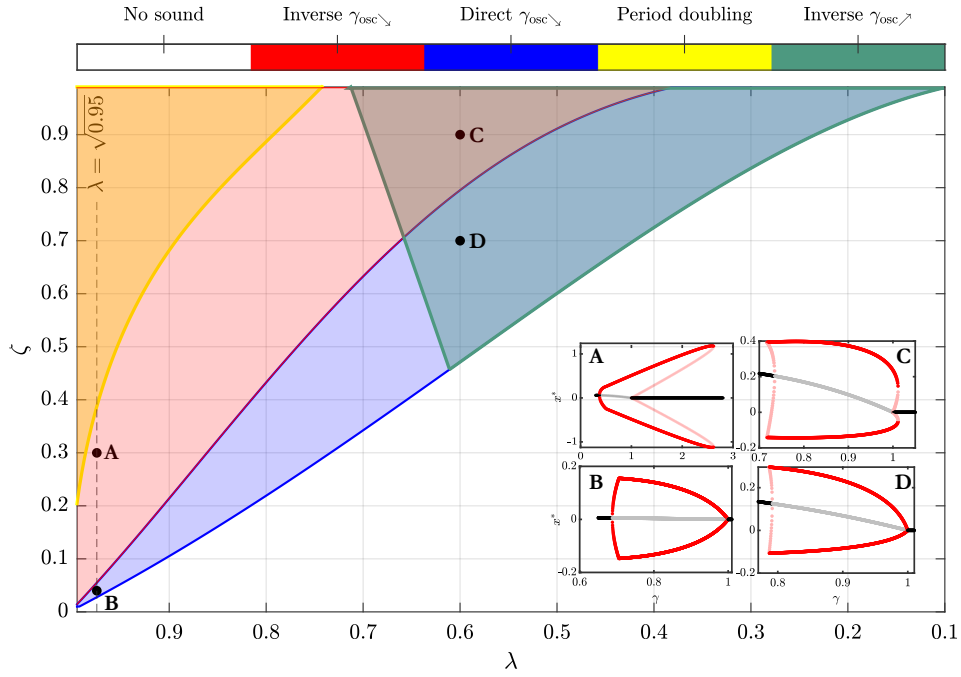


FIG. 5. Evolution of the dynamic behavior of the clarinet with respect to the linear losses parameter  $\lambda$  and to the embouchure parameter  $\zeta$ , without localized nonlinear losses. The nature of the oscillation thresholds  $\gamma_{\text{osc}\nearrow}$  and  $\gamma_{\text{osc}\searrow}$  is indicated for each point in the space  $(\lambda, \zeta)$ . In the white-colored region, the clarinet produces no sound for all  $\gamma$ , whereas sound can be played in the colored regions. In the green region, the bifurcation at  $\gamma_{\text{osc}\nearrow}$  is inverse; outside this region it is direct. In the red region, the bifurcation at  $\gamma_{\text{osc}\searrow}$  is inverse (i.e.  $\gamma_{\text{ext}} > 1$ ); in the blue region it is direct (i.e. the clarinet can not be played higher than  $\gamma = 1$ ). In the yellow region, longer-period regimes  $R_n$  ( $n \geq 3$ ) can be played. The black dots A, B, C and D show the four typical scenarios at  $\gamma_{\text{osc}\nearrow}$  (direct for A and B, inverse for C and D) and at  $\gamma_{\text{osc}\searrow}$  (direct for B and D, inverse for A and C).

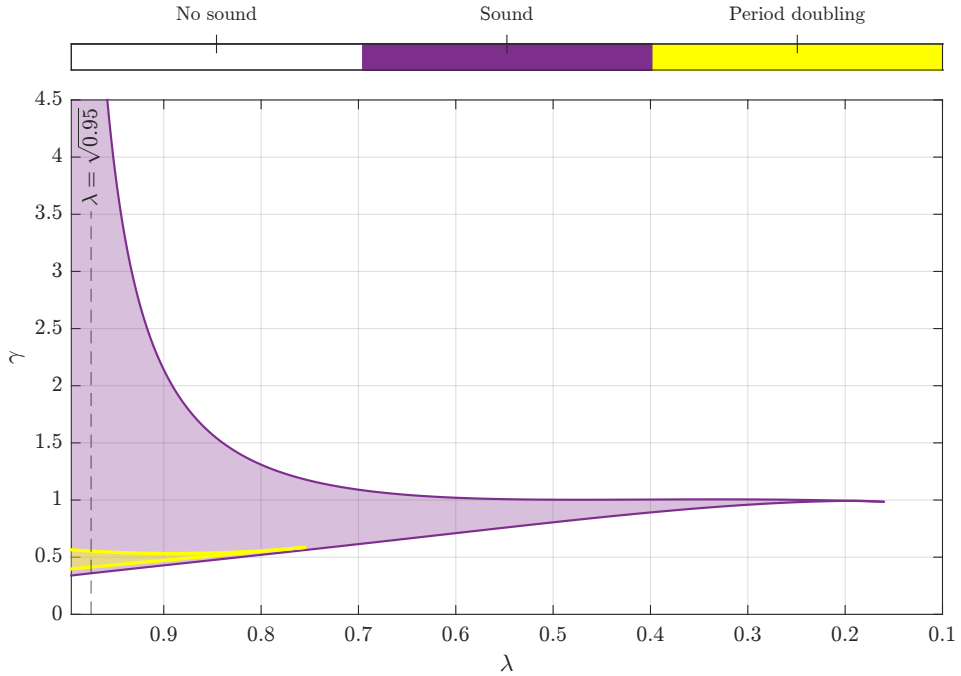


FIG. 6. Evolution of the playing range of the clarinet with respect to the linear losses parameter  $\lambda$  and to the blowing pressure parameter  $\gamma$ , for  $\hat{K}_0 = 0$ . For each value of  $\lambda$ , the values of  $\gamma$  for which there is a value of  $\zeta \in [0, 0.99]$  such that an oscillating regime can be played (two-state regime in purple, longer-period regimes in yellow) or not (in white) are indicated.

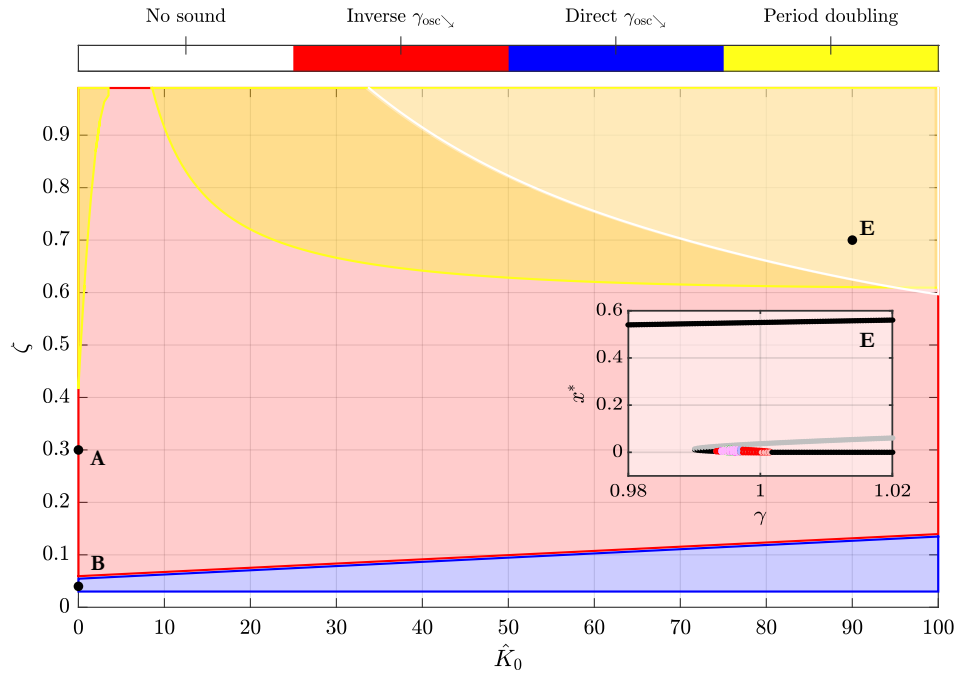


FIG. 7. Same as Figure 5, here in the plane  $(\hat{K}_0, \zeta)$  with  $\lambda = \sqrt{0.95}$ . In the white region at the top right corner, the equilibrium  $R_1$  is stable for all  $\gamma$ , but oscillating regimes are also stable. Point E highlights the multistability between the equilibrium (stable in black/unstable in gray) and the oscillating regimes (stable/unstable  $R_2$  in red/light red, stable  $R_4$  in pink.)

reduce the amplitude of the acoustic pressure without altering too much the value of  $\gamma_{\text{osc}\nearrow}$  nor changing the nature of the bifurcation, as shown on Figure 9. When  $\hat{K}_0$  increases (Fig. 9(a)), the slope of the amplitude of the two-state regime around  $\gamma_{\text{osc}\nearrow}$  decreases, whereas linear losses increase this slope (Fig. 9(b)), ultimately leading to an inverse bifurcation (green zone on Figure 5). Thanks to localized nonlinear losses, the reduction of the slope near  $\gamma_{\text{osc}\nearrow}$  could help clarinetists to control the softest dynamics of their instrument.

## VI. CONCLUSION

The main aim of this study is to contribute to the understanding of nonlinear losses that are localized at the open end of a clarinet-like instrument. The complete system is written as an iterated function, which enables to investigate the stability of the different playing regimes in a simple and systematic way. This work thus follows on from the literature devoted to minimal clarinet models<sup>8,11,19</sup>. As a main result of this study, localized nonlinear losses increase the value of the minimal blowing pressure for which the oscillations start. This effect is not reported in previous works dedicated to this phenomenon<sup>4,6,22</sup>. Although the bore of a real clarinet is much more complicated than a cylindrical tube, this result provides some insight for the wind instrument makers into the value of undercutting the side holes to modify the dynamic range of the instrument. This hypothesis could be explored in a future work thanks to the formu-

lation proposed in Eq. (7), which provides a simple way to take into account localized nonlinear losses in the side hole of a waveguide model. Furthermore, localized nonlinear losses act as a natural compressor, reducing the amplitude of the acoustic pressure without altering the direct nature of the bifurcation at the onset of the oscillations. This is not the case for linear losses, which significantly increase the value of the minimal blowing pressure to produce a sound, and can change the nature of the bifurcation at the onset of the oscillations from direct to inverse. Finally, the increase of nonlinear losses entails the disappearance of high order regimes, before they reappear for very strong values of the coefficient. Future studies may explore experimentally the possible influence of localized nonlinear losses on the control of the nuances from the clarinetist.

## ACKNOWLEDGMENTS

This study has been supported by the French ANR LabCom LIAMFI (ANR-16-LCV2-007-01). The authors warmly thank F. Monteghetti for fruitful preliminary discussions.

## AUTHOR DECLARATIONS AND DATA AVAILABILITY STATEMENT

The authors have no conflicts to disclose. The data that support the findings of the present study are avail-

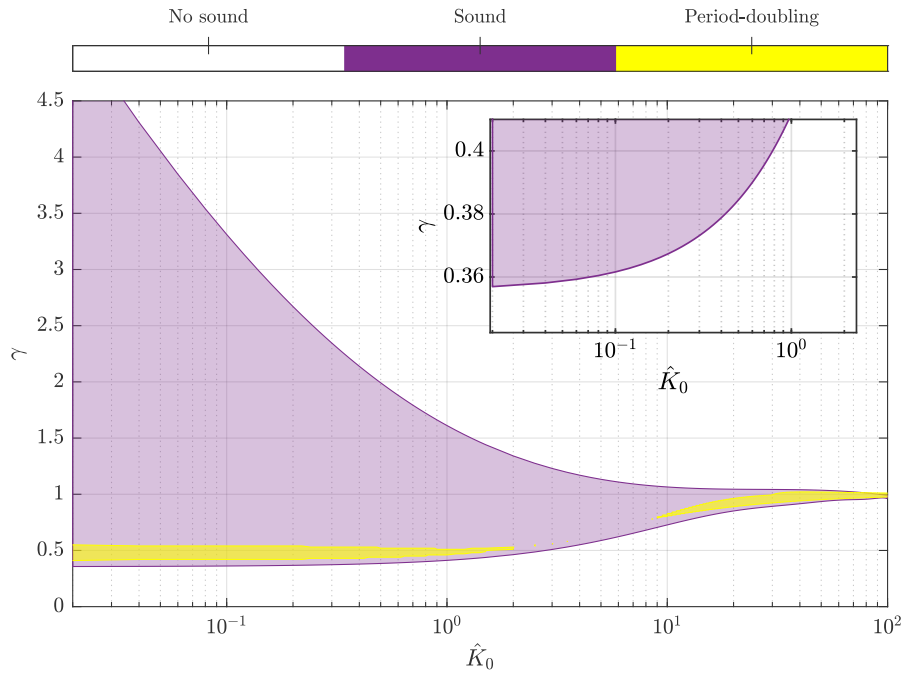


FIG. 8. Same description as Figure 6, in the plane  $(\hat{K}_0, \gamma)$  with  $\lambda = \sqrt{0.95}$ . Here, the x-axis is in logarithmic scale.

able from the corresponding author upon reasonable request.

- <sup>1</sup>A. Chaigne and J. Kergomard, *Acoustics of musical instruments* (Springer, 2016).
- <sup>2</sup>C. Maganza, R. Caussé, and F. Laloë, “Bifurcations, period doublings and chaos in clarinetlike systems,” *Europhysics letters* **1**(6), 295 (1986).
- <sup>3</sup>T. A. Wilson and G. S. Beavers, “Operating modes of the clarinet,” *The Journal of the Acoustical Society of America* **56**(2), 653–658 (1974).
- <sup>4</sup>J.-P. Dalmont and C. Frappé, “Oscillation and extinction thresholds of the clarinet: comparison of analytical results and experiments,” *The Journal of the Acoustical Society of America* **122**(2), 1173–1179 (2007) doi: [10.1121/1.2747197](https://doi.org/10.1121/1.2747197).
- <sup>5</sup>J.-P. Dalmont, J. Gilbert, J. Kergomard, and S. Ollivier, “An analytical prediction of the oscillation and extinction thresholds of a clarinet,” *The Journal of the Acoustical Society of America* **118**(5), 3294–3305 (2005).
- <sup>6</sup>M. Atig, J.-P. Dalmont, and J. Gilbert, “Saturation mechanism in clarinet-like instruments, the effect of the localised non-linear losses,” *Applied Acoustics* **65**(12), 1133–1154 (2004) <https://hal.archives-ouvertes.fr/hal-00474985>.
- <sup>7</sup>B. Bergeot, A. Almeida, B. Gazengel, C. Vergez, and D. Ferrand, “Response of an artificially blown clarinet to different blowing pressure profiles,” *The Journal of the Acoustical Society of America* **135**(1), 479–490 (2014).
- <sup>8</sup>B. Bergeot, A. Almeida, C. Vergez, and B. Gazengel, “Prediction of the dynamic oscillation threshold in a clarinet model with a linearly increasing blowing pressure,” *Nonlinear Dynamics* **73**, 521–534 (2013).
- <sup>9</sup>N. Szwarcberg, T. Colinot, C. Vergez, and M. Jousserand, “Amplitude-dependent modal coefficients accounting for localized nonlinear losses in a time-domain integration of woodwind model,” *Acta Acustica* **7**, 16 (2023).
- <sup>10</sup>D. H. Keefe, “Acoustic streaming, dimensional analysis of nonlinearities, and tone hole mutual interactions in woodwinds,” *The*

*Journal of the Acoustical Society of America* **73**(5), 1804–1820 (1983).

- <sup>11</sup>P.-A. Taillard, J. Kergomard, and F. Laloë, “Iterated maps for clarinet-like systems,” *Nonlinear dynamics* **62**, 253–271 (2010).
- <sup>12</sup>U. Ingård and S. Labate, “Acoustic circulation effects and the nonlinear impedance of orifices,” *The Journal of the Acoustical Society of America* **22**(2), 211–218 (1950).
- <sup>13</sup>J. Disselhorst and L. Van Wijngaarden, “Flow in the exit of open pipes during acoustic resonance,” *Journal of Fluid Mechanics* **99**(2), 293–319 (1980).
- <sup>14</sup>D. K. Singh and S. W. Rienstra, “Nonlinear asymptotic impedance model for a helmholtz resonator liner,” *Journal of Sound and Vibration* **333**(15), 3536–3549 (2014).
- <sup>15</sup>A. Komkin, A. Bykov, and M. Mironov, “Experimental study of nonlinear acoustic impedance of circular orifices,” *The Journal of the Acoustical Society of America* **148**(3), 1391–1403 (2020).
- <sup>16</sup>M. Peters, A. Hirschberg, A. Reijnen, and A. Wijnands, “Damping and reflection coefficient measurements for an open pipe at low mach and low helmholtz numbers,” *Journal of Fluid Mechanics* **256**, 499–534 (1993).
- <sup>17</sup>F. Monteghetti, “Analysis and discretization of time-domain impedance boundary conditions in aeroacoustics,” Ph.D. thesis, Institut Supérieur de l’Aéronautique et de l’Espace (ISAE-SUPAERO), 2018.
- <sup>18</sup>P. Guillemain and J. Terroir, “Digital synthesis models of clarinet-like instruments including nonlinear losses in the resonator,” in *9th International Conference on Digital Audio Effects* (2006), p. 83.
- <sup>19</sup>P.-A. Taillard and J. Kergomard, “An analytical prediction of the bifurcation scheme of a clarinet-like instrument: Effects of resonator losses,” *Acta Acustica united with Acustica* **101**(2), 279–291 (2015).
- <sup>20</sup>S. Karkar, C. Vergez, and B. Cochelin, “Oscillation threshold of a clarinet model: A numerical continuation approach,” *The Journal of the Acoustical Society of America* **131**(1), 698–707 (2012).
- <sup>21</sup>M. Atig, J.-P. Dalmont, and J. Gilbert, “Termination impedance of open-ended cylindrical tubes at high sound pressure level,”

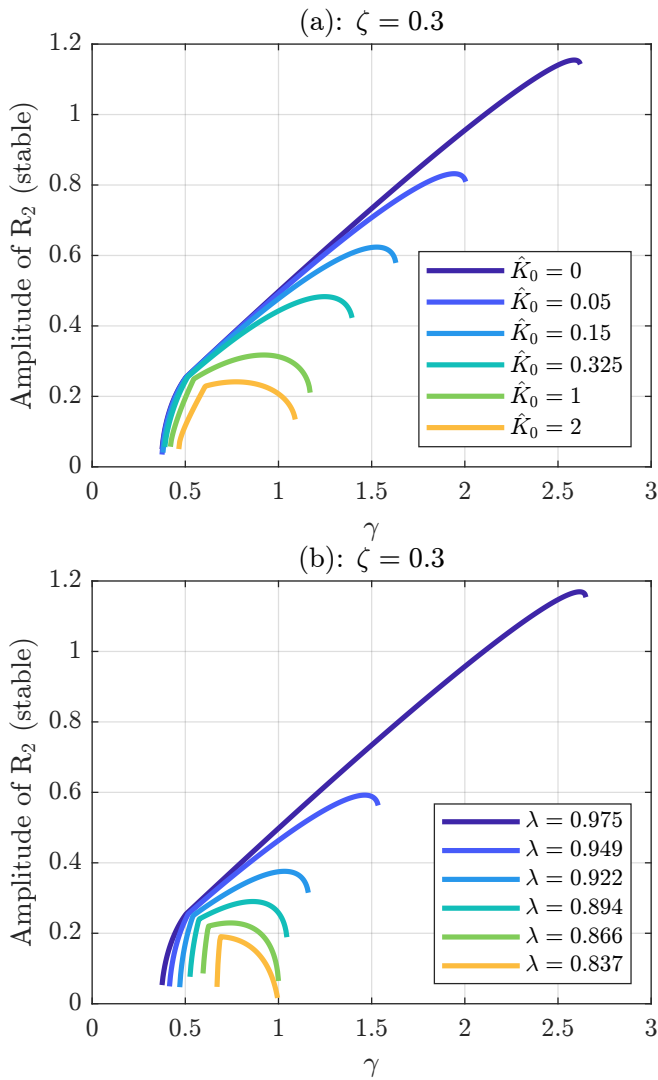


FIG. 9. Evolution of the amplitude of  $R_2$  (when stable) with respect to the blowing pressure  $\gamma$ , for  $\zeta = 0.3$ . (a): variation of  $\hat{K}_0$ ,  $\lambda = \sqrt{0.95}$ . (b): variation of  $\lambda$ ,  $\hat{K}_0 = 0$ .

Comptes Rendus Mécaniques de l'Académie des sciences **332**(4), 299–304 (2004).

<sup>22</sup>P. Guillemain, J. Kergomard, and T. Voinier, “Real-time synthesis of clarinet-like instruments using digital impedance models,” *The Journal of the Acoustical Society of America* **118**(1), 483–494 (2005).

<sup>23</sup>N. Szwarcberg, T. Colinot, C. Vergez, and M. Jousserand, “Modal decomposition synthesis for localized nonlinear losses at termination of a woodwind model: influence on sound characteristics,” in *Forum Acusticum 2023*, European Acoustics Association (EAA), Turin (IT), Italy (2023), p. <https://www.fa2023.org/>, <https://hal.science/hal-04379983>.

## LIST OF FIGURES

- 1 Evolution of the shape of  $\hat{r}_{n1}$  when increasing  $\hat{K}_0$  (values are displayed on the figure), with  $\lambda = \sqrt{0.95}$ . . . . . 3
- 2 Evolution of  $f$  when increasing  $\hat{K}_0$  (values are displayed on the figure), with  $\lambda = \sqrt{0.95}$ ,  $\gamma = 0.4$  and  $\zeta = 0.5$ . . . . . 3
- 3 Limit of stability of  $R_1$  (in black) and  $R_n$  ( $n > 2$ , in blue) in the  $(\gamma, \zeta, \hat{K}_0)$  space, for  $\lambda = \sqrt{0.95}$ . The non-oscillating state is stable outside the volume delimited by the black surface, and unstable inside. The three dashed-line curves are horizontal cuts at  $\hat{K}_0 = \{1, 5, 10\}$ . The two dotted-line curves are horizontal cuts at  $\hat{K}_0 = \{35, 70\}$ . The long-period regimes are unstable outside the volume delimited by the blue surface. Other views and cross-sections are shown in the Supplementary Figure 2. . . . . 5
- 4 Stability region of  $R_2$  in the  $(\gamma, \zeta)$  plane, for different values of  $\hat{K}_0 \in [0, 2]$  and  $\lambda = \sqrt{0.95}$ . The values of  $\hat{K}_0$  corresponding to the different colors are written on the figure. On the left panel, the color patches are superimposed in a fan shape from blue ( $\hat{K}_0 = 0$ ) to yellow ( $\hat{K}_0 = 2$ ). On the right panel, a detailed view is given on the region where  $R_2$  is unstable and  $R_n$  is stable. . . . . 6
- 5 Evolution of the dynamic behavior of the clarinet with respect to the linear losses parameter  $\lambda$  and to the embouchure parameter  $\zeta$ , without localized nonlinear losses. The nature of the oscillation thresholds  $\gamma_{osc \nearrow}$  and  $\gamma_{osc \searrow}$  is indicated for each point in the space  $(\lambda, \zeta)$ . In the white-colored region, the clarinet produces no sound for all  $\gamma$ , whereas sound can be played in the colored regions. In the green region, the bifurcation at  $\gamma_{osc \nearrow}$  is inverse; outside this region it is direct. In the red region, the bifurcation at  $\gamma_{osc \searrow}$  is inverse (i.e.  $\gamma_{ext} > 1$ ); in the blue region it is direct (i.e. the clarinet can not be played higher than  $\gamma = 1$ ). In the yellow region, longer-period regimes  $R_n$  ( $n \geq 3$ ) can be played. The black dots A, B, C and D show the four typical scenarios at  $\gamma_{osc \nearrow}$  (direct for A and B, inverse for C and D) and at  $\gamma_{osc \searrow}$  (direct for B and D, inverse for A and C). . . . . 7

6	Evolution of the playing range of the clarinet with respect to the linear losses parameter $\lambda$ and to the blowing pressure parameter $\gamma$ , for $\hat{K}_0 = 0$ . For each value of $\lambda$ , the values of $\gamma$ for which there is a value of $\zeta \in [0, 0.99]$ such that an oscillating regime can be played (two-state regime in purple, longer-period regimes in yellow) or not (in white) are indicated. ....	7
7	Same as Figure 5, here in the plane $(\hat{K}_0, \zeta)$ with $\lambda = \sqrt{0.95}$ . In the white region at the top right corner, the equilibrium $R_1$ is stable for all $\gamma$ , but oscillating regimes are also stable. Point E highlights the multistability between the equilibrium (stable in black/unstable in gray) and the oscillating regimes (stable/unstable $R_2$ in red/light red, stable $R_4$ in pink.) ....	8
8	Same description as Figure 6, in the plane $(\hat{K}_0, \gamma)$ with $\lambda = \sqrt{0.95}$ . Here, the x-axis is in logarithmic scale. ....	9
9	Evolution of the amplitude of $R_2$ (when stable) with respect to the blowing pressure $\gamma$ , for $\zeta = 0.3$ . (a): variation of $\hat{K}_0$ , $\lambda = \sqrt{0.95}$ . (b): variation of $\lambda$ , $\hat{K}_0 = 0$ . ...	10